# HPU/iron oxide nanoparticles decorated RGO nanocomposite as multi-stimuli responsive self-healing and shape memory materials

## Highlights

This chapter deals with the preparation, characterization and property evaluation of HPU/iron oxide-reduced graphene oxide nanocomposite. This nanocomposite is investigated here as a multi-stimuli responsive self-healing and shape memory material. Iron oxide- reduced graphene oxide nanohybrid was prepared by simultaneous reduction of GO by *C. esculenta* leaf extract and formation of iron oxide nanoparticles by coprecipitation method by using banana peel ash extract as the base source. The prepared nanohybrid and nanocomposite were characterized by different spectroscopic and analytical tools. The fabricated nanocomposite exhibited good thermal and mechanical properties. In addition, the nanocomposite demonstrated rapid and repeatable self-healing abilities under exposure of MW and direct sunlight. It also showed excellent shape-recovery ability under the same stimuli. Thus, the work contributes a light in the field of advanced smart materials.

## 4.1. Introduction

The self-healing ability is a crucial feature of biomaterials and increases the durability of natural materials, whereas man-made materials are susceptible to failure upon encountering damage or fracture by external factors during their service life.[1] Thus, the development of self-healing materials which can repair themselves after mechanical damage are attracted greatly over the past decade.[2-4] Thus, a variety of methods are attempted to develop self-healing materials, especially self-healing polymers (SHPs). Recently, most of SHPs are developed based on encapsulation and reversible chemistry with covalent and non-covalent chemical bonds.[5-8] The encapsulation approach is achieved by the incorporation of microcapsule containing a healing agent, which readily polymerizes in the damaged area upon release from the microcapsules.[9,10] Although this approach shows a great potential for internal healing, it fails to heal macroscopic damages. In addition, the irreversible healing nature is another inadequacy of it. However, this limitation can be overcome by using reversible chemistry.[11] Intermolecular interactions and reversible bonds are useful to introduce the healing ability of a polymer for multiple times. Despite their great advances, some serious problems again limit their practical applicability. The reversible polymers suffer from poor mechanical properties, along with high costs.[12,13]

Thus, the development of a novel SHP with repeated healing efficiency and outstanding mechanical properties is still a key challenge. To address this problem, Huang and co-workers designed a PU/graphene nanocomposite as a SHP which demonstrated repeated healing efficiency by infrared (IR) light, electricity and MW energy with good mechanical properties.[14] However, to achieve such healing properties, the amount of graphene, as well as the MW power consumption, is quite high. Thus, the use of such stimuli is difficult in practical field of applications. Thus, emerging materials with a rapid and repeatable self-healing capability with adequate mechanical properties still remain a daunting challenge.

At this juncture, it is important to mention that a new concept is developed that uses SMP for an improvement of the self-healing process.[15] SMP provides a mechanism to partially or fully heal the crack and helps to repair it. Michal et al. prepared a polymer with a structurally dynamic polydisulfide network that exhibited both shape memory and self-healing properties.[16] This polydisulfide network demonstrated thermo shape-memory and photohealable properties. Also, Wang et al. fabricated polyethylene–carbon black

nanocomposite, which showed improved self-healing by a shape-memory effect.[17] However, these materials unable to show multi-stimuli responsive behavior.

In this context, the previous chapter proved the potentiality of HPU/RGO nanocomposite as a multi-stimuli responsive shape-memory material under MW, sunlight and thermal energy. Therefore, the present nanocomposite may be the right choice to fabricate a self-healing material. In addition, the use of iron oxide–RGO (IO–RGO) nanohybrid instead of RGO only exhibits some additional advantages, as IO nanoparticles possess good thermal conductivity, magnetic behavior and MW absorbing capacity.[18,19] Furthermore, RGO is well-known for its good MW and sunlight absorbing capacity, excellent thermal conductivity, etc. as discussed in the previous chapter.[19,20] Therefore, IO-RGO nanohybrid can be used to enjoy their combined effects.

Thus, in the present study, IO-RGO nanohybrid was prepared by a greener one-pot technique and a self-healing elastomeric HPU nanocomposite was fabricated using the IO-RGO nanohybrid. The prepared nanohybrid and nanocomposite were characterized, and the mechanical properties, multi-stimuli self-healing and shape-memory behavior of the nanocomposite under sunlight and MW stimuli were also evaluated.

## 4.2. Experimental

### 4.2.1. Materials

The monoglyceride of the castor oil, TDI, PCL and BD used for the preparation of HPU were same as described in Chapter 2, section 2.2.1. The same GO, ferric chloride anhydrate and *C. esculenta* leaf extract as reported in sub-chapter 3A, were used for the preparation of IO-RGO nanohybrid.

Ferrous chloride tetrahydrate was purchased from Merck, Germany. The minimum assay is 99.0%. Its molar mass and melting point are 198.81 g/mol and 105 °C. It is widely used as a reducing flocculating agent in wastewater treatment, especially for chromate containing wastes. It was used as a precursor for the preparation of IO-RGO nanohybrid.

Banana (*Musa acuminata*) peels were collected from Tezpur University campus, Assam, India for the preparation of peel ash aqueous extract. Firstly, the banana peels were dried under sunlight for 7 days and then the dried peels were burned in a furnace at 650 °C. The ash was collected after complete burning of the peels. Then, the ash was mixed with water by thorough stirring and finally filtered it. The filtrate was taken as the aqueous base extract for the preparation of IO nanoparticles in the nanohybrid.

### 4.2.2. Characterization

FTIR, XRD, DSC and TGA analyses, and mechanical tests were performed under the same conditions and by using the same instruments as described in Chapter 2, section 2.2.2. Raman spectra of IO-RGO were taken by same Raman spectroscope and same condition as mentioned in sub-chapter 3A, section 3A.2.2. The morphology and SAED pattern of IO-RGO nanohybrid and HPU/IO-RGO nanocomposite were analyzed by same HRTEM as mentioned in sub-chapter 3A, section 3A.2.2. Shape memory test under MW and sunlight was performed as mentioned in the sub-chapter 3C, section 3C.2.2. The same domestic MW oven was used to test the shape memory and self-healing properties of the nanocomposite as mentioned in sub-chapter 3C, section 3C.2.2. The intensity of the solar light was measured by using a lux meter (LX-101, Lutron, Taiwan).

In order to evaluate the healing performance, films with a thickness of 0.5 mm of the nanocomposite were cut (10 $mm^3$ × 0.2 $mm^3$ × 0.015 $mm^3$ in dimension) in a transverse direction by a razor blade, and the cracked was healed by sunlight and MW, separately. The healing efficiency was calculated as the ratio of the tensile strength values of the nanocomposites before and after healing. The tensile strengths of the pristine and the healed samples were measured by the same UTM. The tensile strengths of pristine HPU, as well as the nanocomposites with different loadings of the nanohybrid, were measured for at least five samples in each case, before and after the healing process. The optimal healing time for each case was defined as the shortest time required to achieve the best healing efficiency under the given conditions. Three different MW powers (180 W, 360 W and 540 W) were used for the healing. The healing under sunlight was performed using direct sunlight (11 am−2 pm) at Tezpur University campus in the month of November on sunny days [average temperature (29 ± 1 °C) and humidity (65 ± 1%)], with a light with a light intensity of 90000–100000 lux.

### 4.2.3. Preparation of IO-RGO nanohybrid

IO-RGO nanohybrid was prepared by a greener one-pot technique. Briefly, an amount of 50 mg of GO was dispersed in 50 mL water by sonication for 30 min. The suspension was then mixed with 64.8 mg of anhydrate $FeCl_3$ and 39.6 mg of $FeCl_2.4H_2O$ by constant stirring for 1 h under the $N_2$ atmosphere. Then 20 mL of banana peel ash extract and 10 mL of *C. esculenta* leaf aqueous extract were added into the above suspension and stirred for 30 min to reduce GO and to form IO nanoparticles.

## 4.2.4. Preparation of HPU/IO-RGO nanocomposite

HPU/IO-RGO nanocomposite was prepared following the same method which was used to prepare HPU/RGO nanocomposite in the sub-chapter 3C, section 3C.2.4. Only required amounts of dispersed IO-RGO nanohybrid in DMAc (different wt%: 0.5, 1 and 2 with respect to total weight of nanocomposite) were incorporated instead of RGO in 1$^{st}$ step of the polymerization reaction to obtain *in situ* HPU/IO-RGO nanocomposite. The nanocomposites with 0.5 wt%, 1 wt% and 2 wt% of IO-RGO nanohybrid were encoded as HPU/IO-RGO0.5, HPU/IO-RGO1 and HPU/IO-RGO2, respectively.

## 4.3. Results and discussion

### 4.3.1. Preparation of IO-RGO nanohybrid

IO-RGO nanohybrid was prepared by simultaneously reduction of GO by *C. esculenta* leaf aqueous extract and chemical deposition of iron ions (ferrous and ferric ions) which further formed IO nanoparticles by using banana peel ash aqueous extract as a base source under ambient conditions. The polyphenol compounds (presence in the *C. esculenta* leaf extract) act as nucleophiles and reduce the oxygenating groups of GO as shown in the Scheme 3A.1 (sub-chapter 3A, section 3A.3.9). Also, the polyphenol compounds form complexes with the ferrous and ferric ions and hence, high amount of $H^+$ and electrons are released which further assist in the reduction process as stated in sub-chapter 3A, section 3A.3.9. As a result, GO sheets were effectively reduced in the nanohybrid at room temperature within 30 min. GO contains sufficient amounts of polar functional groups as mentioned in sub-chapter 3A, section 3A.3.3. These groups help to capture the ferrous and ferric ions which form IO nanoparticles by co-precipitation method as shown in **Scheme 4.1**.[21]
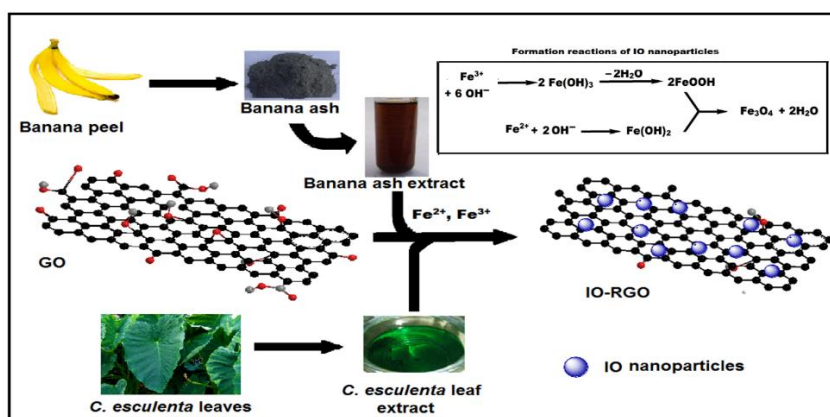


**Scheme 4. 1** Preparation of IO-RGO nanohybrid

Even after the reduction of GO, a few functional groups (mainly hydroxyl group) are still remained which provide the stability of IO nanoparticles on the surface of RGO sheet. Further, the surface of the IO nanoparticles contains a few adsorbed water molecules.[22] Thus, a number of polar-polar and H-bonding interactions between IO nanoparticles and RGO sheet occurred to stabilize the nanoparticles on RGO sheet.[22]

### 4.3.2. Characterization of IO-RGO nanohybrid

The crystalline structures for the pure IO nanoparticles and IO-RGO nanohybrid were confirmed by XRD patterns as shown in **Figure 4.1**. The diffraction peaks of the pure IO nanoparticles observed at 2θ=30.15, 36.2, 43.32, 53.89, 57.13 and 62.29° correspond to (220), (311), (400), (422), (511) and (440) crystal planes, respectively.[23] The appearance of peaks agrees with the standard XRD data for the cubic spinel crystal with a face-centered cubic (fcc) structure of magnetite particles (JCPDS file no. 89-3854). The presence of a new broad diffraction peak at 2θ= 26° reflected the presence of (002) plane of graphitic structure similar to CRGO (sub-chapter 3A, section 3A.3.4). All characteristic diffraction peaks of IO nanoparticles were present in the diffraction pattern of IO-RGO nanohybrid.
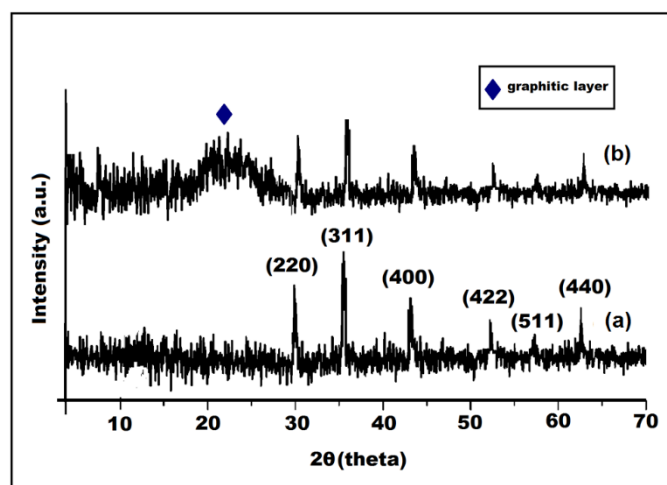


**Figure 4.1** XRD patterns of (a) IO nanoparticles and (b) IO-RGO nanohybrid

FTIR spectra of GO and IO-RGO nanohybrid are shown in **Figure 4.2**. A significant decreased in the intensity of peaks of GO at around 3400 cm$^{-1}$ (for H-bonded hydroxyl group), 1049 cm$^{-1}$ (for C–O stretching) and 1204 cm$^{-1}$ (for C–O–C stretching), complete diminish of C=O stretching peak at 1720 cm$^{-1}$, and the presence of a new stretching vibration

of Fe–O at 556 cm$^{-1}$ suggest the reduction of the oxygen-containing groups in GO and existence of IO nanoparticles in IO-RGO nanohybrid.[24]
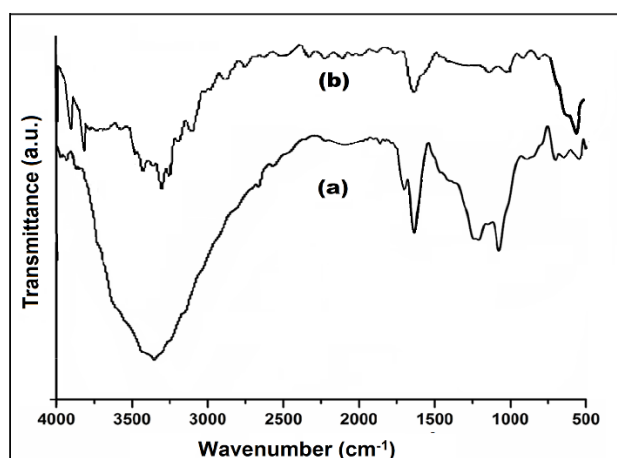


**Figure 4.2** FTIR spectra of (a) GO and (b) IO-RGO nanohybrid [spectra of GO is used from sub-chapter 3A for better comparison]

The D vibration modes of GO and IO-RGO nanohybrid were appeared at 1322 and 1326 cm$^{-1}$, respectively and G vibration modes of GO and IO-RGO nanohybrid were found at 1587 and 1582 cm$^{-1}$, respectively (**Figure 4.3**). The increased in $I_D/I_G$ ratio from 0.88 to 1.1 indicates the reduction of GO in IO-RGO nanohybrid. The typical peak of magnetite was also observed at 528 cm$^{-1}$ in the spectra of the nanohybrid, corresponding with the reported magnetite spectrum.[25] The 2D peak at around 2685 cm$^{-1}$ implies the presence of few-layers RGO in IO-RGO nanohybrid.[26]
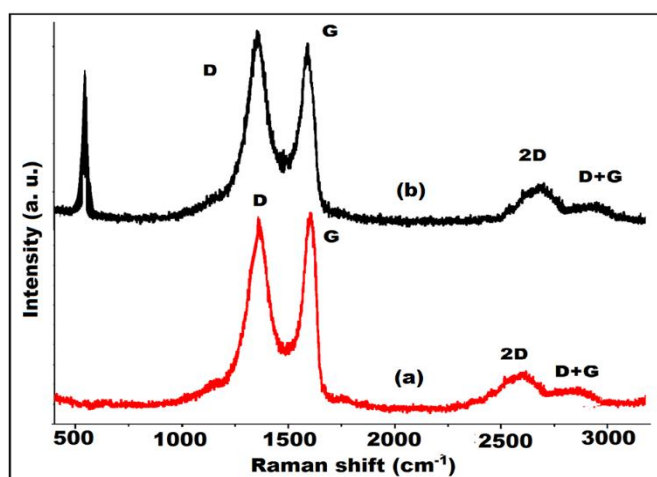


**Figure 4.3** Raman spectra of (a) GO and (b) IO-RGO nanohybrid [spectra of GO is used from sub-chapter 3A for better comparison]

TGA was employed to evaluate the amount of IO nanoparticles present in the nanohybrid. The thermogram of IO-RGO nanohybrid displayed a significant weight loss at about 480 °C and a constant weight above 580 °C (**Figure 4.4**). This is due to pyrolysis of the remaining oxygenating groups and burning of ring carbon presence in RGO sheet in the nanohybrid. The slight weight loss below 220 °C could probably be attributed to the evaporation of adsorbed unstable phytochemicals as well as water molecules. Therefore, the weight residue of about 53% in TGA is mainly due to mass percentage of IO nanoparticles present in IO-RGO nanohybrid.[27]
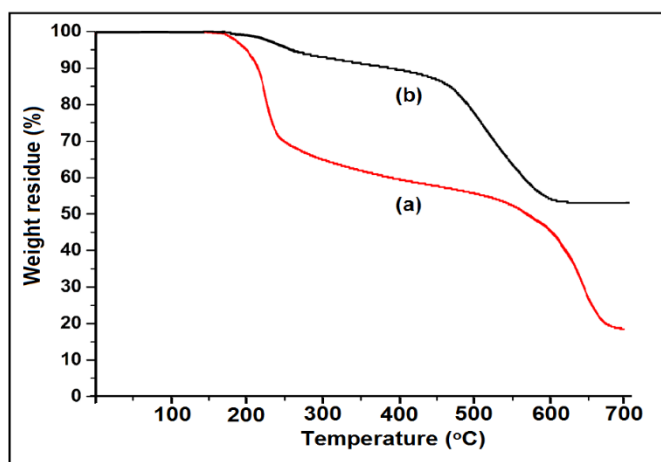


**Figure 4.4** TGA thermograms of (a) GO and (b) IO-RGO nanohybrid [spectra of GO is reproduced from sub-chapter 3A for better comparison]

TEM images depict the decoration of IO nanoparticles on RGO sheet with a narrow size distribution and uniform dispersion (**Figure 4.5**). The typical particle size is in the range of 10-25 nm with the most frequent particles size being within the range 10-15 nm.
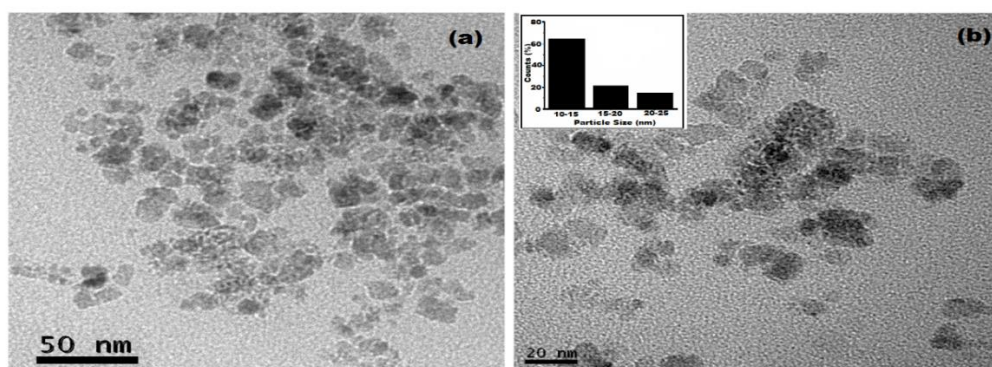


**Figure 4.5** HRTEM images of IO-RGO nanohybrid (a) at low and (b) at high resolution

The magnetic properties of IO nanoparticles and IO-RGO nanohybrid were studied at room temperature by VSM. The saturation magnetization ($M_s$) values of IO nanoparticles and IO-RGO nanohybrid were found to be 76 and 34 emu $g^{-1}$ (at an applied magnetic field of 20 kOe) (**Figure 4.6**). The magnetization value of IO-RGO nanohybrid was lesser than IO nanoparticles due to the presence of nonmagnetic RGO (carbonaceous material).[24] Both IO nanoparticles and IO-RGO nanohybrid exhibited superparamagnetic like behavior at room temperature with small coercivity and remanence.
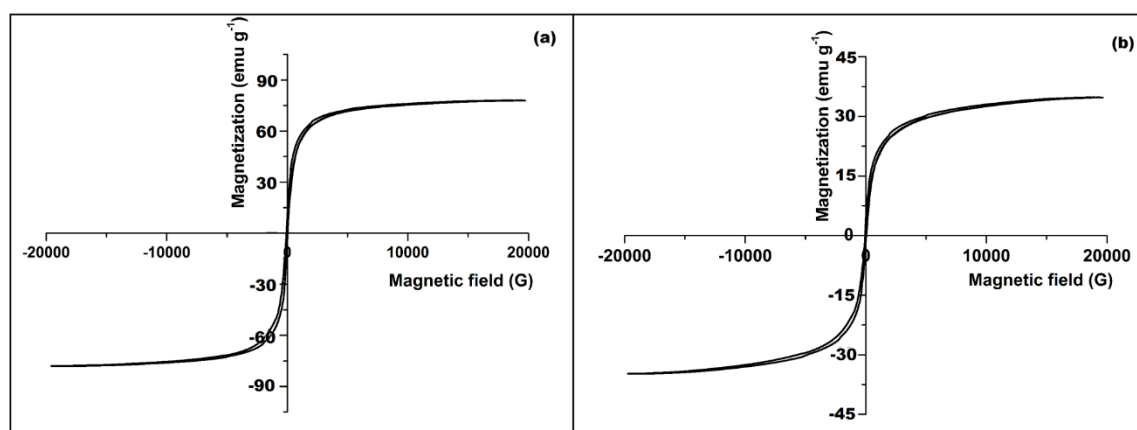


**Figure 4.6** Hysteresis loops of (a) IO nanoparticles and (b) IO-RGO nanohybrid at room temperature

### 4.3.3. Preparation of HPU/IO-RGO nanocomposite

The degree of interaction HPU and nanohybrid mainly relies on the level of dispersion of the nanohybrid into HPU matrix. The homogenous dispersion depends on various factors such as the formation method of nanocomposite, nature of nanomaterials, surface functionalities of polymer and nanomaterials, and mainly the compatibility between the polymeric matrix and the nanomaterial.[28] Among all the available methods for the fabrication of nanocomposite, *in situ* technique is found to be the best as it leads to the homogenous mixing of the nanomaterial into the matrix as discussed in Chapter 1, section 1.3.2.4. Thus, an *in situ* technique was used to prepare HPU/IO-RGO nanocomposite by using the monoglyceride of castor oil as a branch generating moiety and IO-RGO nanohybrid as the reinforcing nanomaterial, as shown in **Scheme 4.2**. The crucial monitoring factors during nanocomposite preparation are the concentration of the reactants (especially the multifunctional moiety), the addition rate of the multifunctional moiety, reaction time, and temperature as mentioned in Chapter 2, section 2.3.1.[29] During the nanocomposite

preparation, the dispersion of the IO-RGO nanohybrid in DMAc was incorporated in the 1st step of the polymerization to obtain a strong interfacial interaction (covalent and noncovalent, shown in **Scheme 4.1**) with HPU chains. In the 2nd step of the reaction, the multifunctional moiety was slowly added in a very dilute solution (15% in xylene) to avoid gel formation, and also temperature of the reaction was gradually raised to 110 °C.
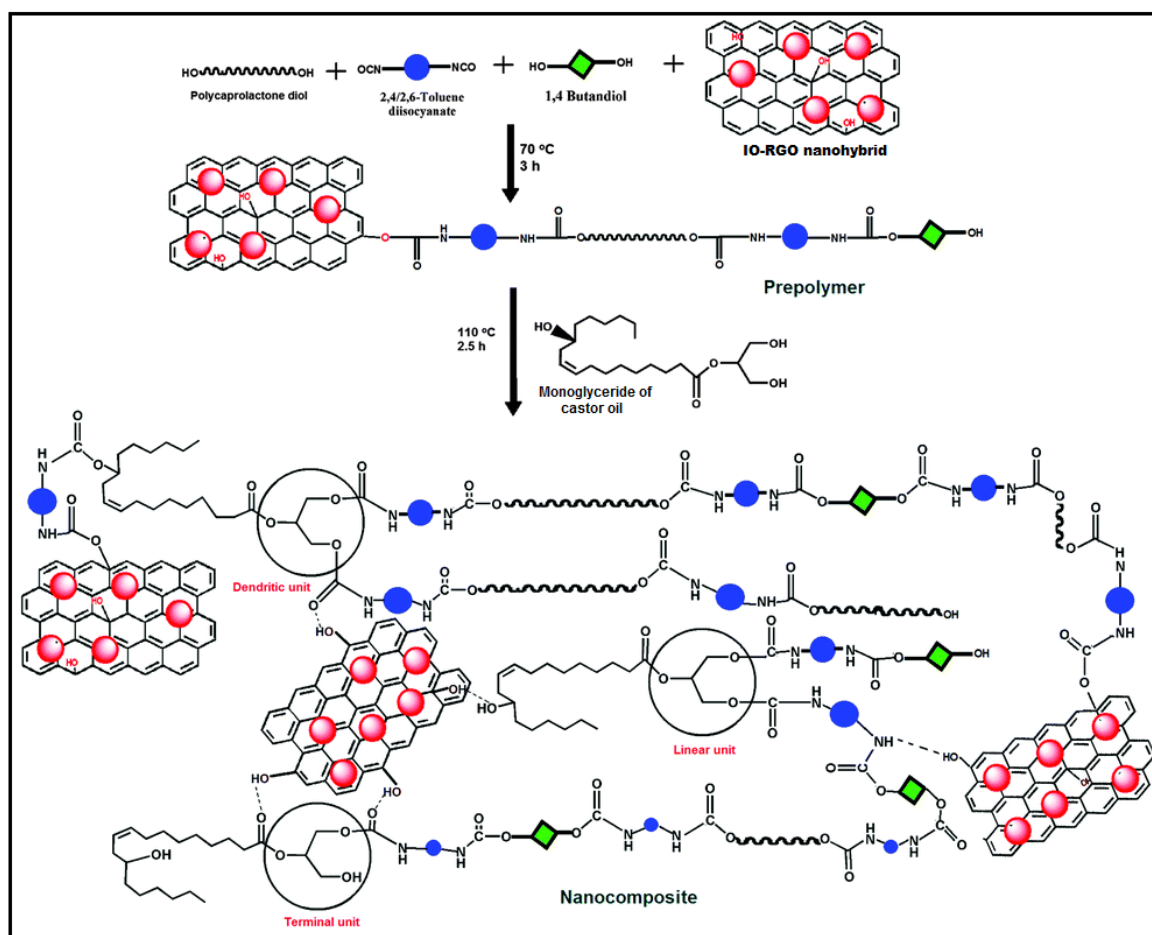


**Scheme 4.2** Preparation of HPU/IO-RGO nanocomposite

### 4.3.4. Characterization of HPU/IO-RGO nanocomposite

FTIR spectra of HPU/IO-RGO nanocomposites are shown in **Figure 4.7**. The appearance of characteristic bands of urethane linkage (as mentioned in Chapter 2, section 2.3.2.) suggests the formation PU. The shifting of the C=O band to 1685 cm$^{-1}$ from 1695 cm$^{-1}$ was observed with the increasing amount of IO-RGO nanohybrid in the nanocomposite similar to other studied nanocomposites. This indicates the presence of interactions among HPU chains and the IO-RGO nanohybrid.[29] These interactions increase with the nanohybrid content.
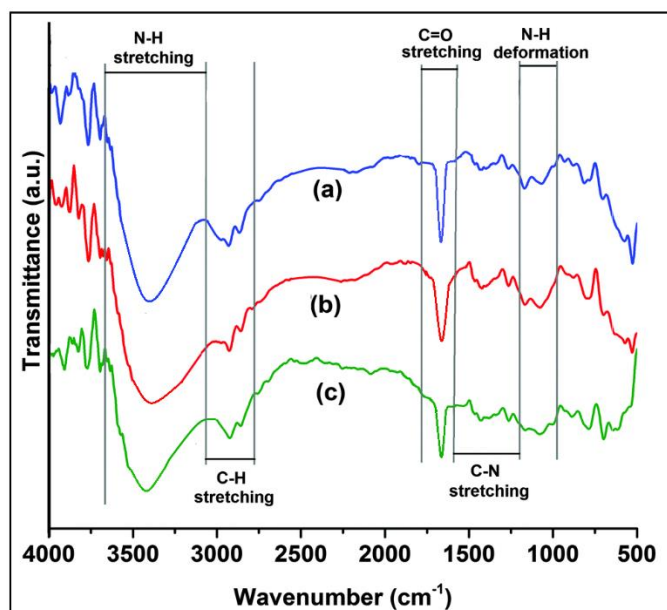
**Figure 4.7** FTIR spectra of (a) HPU/IO–RGO0.5, (b) HPU/IO–RGO1 and (c) HPU/IO–RGO2

All the nanocomposites exhibited two distinct peaks at $2\theta = 21.1°$ (corresponding to a d-spacing of 0.41 nm) and 23.5° (corresponding to a d-spacing of 0.375 nm) similar to HPU (as mentioned in Chapter 2, section 2.3.2.). After incorporation of the nanohybrid, a slight shifting of the PCL peaks towards a higher angle was observed (**Figure 4.8**), which may be due to formation of a more dense structure compared to the pristine HPU similar to other studied nanocomposites in previous chapter.[30]
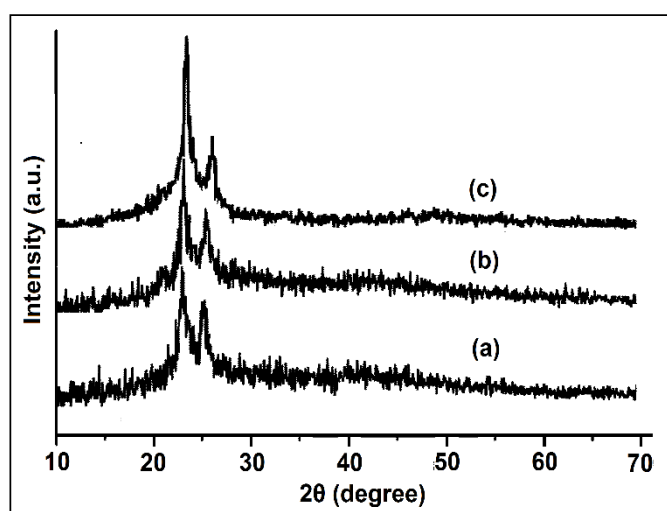


**Figure 4.8** XRD patterns of (a) HPU/IO–RGO0.5, (b) HPU/IO–RGO1 and (c) HPU/IO–RGO2

Also the peak intensity of the PCL moiety was slightly increased with the nanohybrid loading. This indicates that the crystallinity of the nanocomposite increased with the nanohybrid content, as the nanohybrid acts as a nucleating agent. Here, it is pertinent to mention that no such distinct peak is observed for IO-RGO nanohybrid in the XRD patterns of the nanocomposites similar to HPU/RGO nanocomposite. This may be due to the presence of a small amount of nanohybrid in the nanocomposite.

HRTEM was employed to investigate the dispersion of the nanohybrid. HRTEM images of HPU/IO–RGO2 are shown in **Figure 4.9**. From the figure, it is clear that the nanohybrid is finely distributed in HPU matrix. This can be attributed to the good interfacial interaction between the nanoparticles and the polymer matrix.
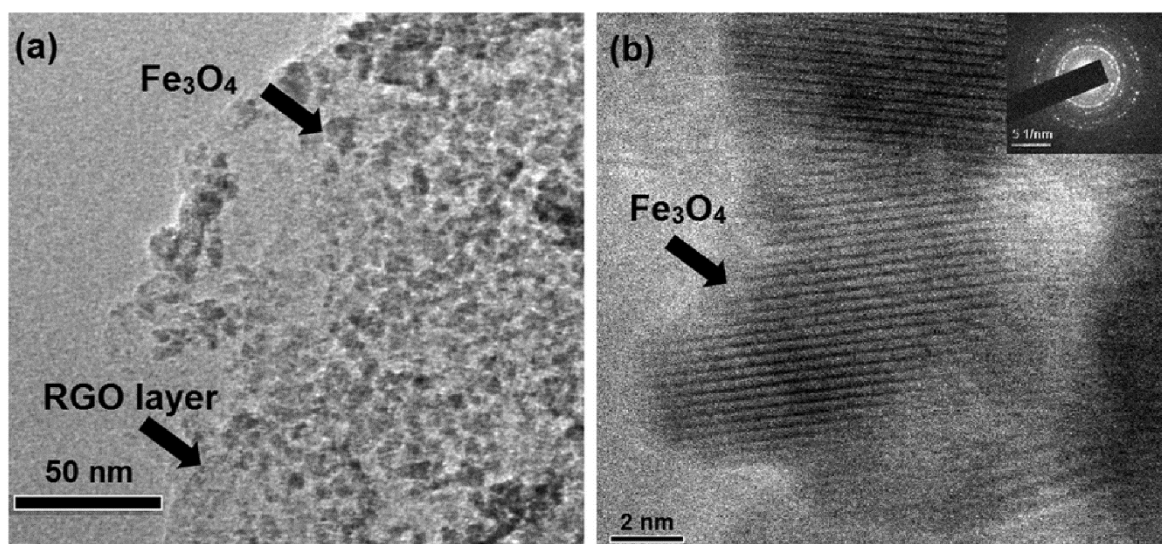


**Figure 4.9** HRTEM images of HPU/IO–RGO2: (a) at low resolution showing RGO layer and decorated IO nanoparticles and (b) at high resolution showing an individual IO nanoparticles on a RGO sheet (inset shows SAED patterns)

### 4.3.5. Mechanical properties of HPU/IO-RGO nanocomposite

After incorporation of the IO-RGO nanohybrid, all the nanocomposites exhibited excellent dose-dependent mechanical properties, like tensile strength, tensile modulus and toughness (**Table 4.1**). HPU/IO-RGO nanocomposites exhibited the simultaneous improvement of tensile strength and elongation at break similar to HPU/RGO nanocomposites. Thus, HPU/IO-RGO nanocomposites show high toughness, scratch hardness and impact strength. Such outstanding mechanical properties can definitely be attributed to the strong interfacial adhesion and good compatibility between HPU and the nanohybrid.[31,32] Also, the remaining

hydroxyl groups in the nanohybrid may react with an isocyanate-terminated prepolymer chain to form a urethane linkage between HPU and the nanohybrid. These strong chemical bonds help to achieve a successful transfer of the load from HPU to the nanohybrid in the nanocomposite. The hard domain of HPU is stiffened due to the presence of the afore-stated covalent bonding, H-bonding, and polar–polar interaction between the nanohybrid and HPU chains.[33] This consequently enhances the tensile modulus of the nanocomposite. The nanocomposite also demonstrated a high dose-dependent toughness after incorporation of the nanohybrid. These nanocomposites also exhibited excellent flexibility with very high elongation at break.

**Table 4.1** Mechanical properties of HPU/IO-RGO nanocomposite

| Property | HPU/IO–RGO0.5 | HPU/IO–RGO1 | HPU/IO–RGO2 |
|---|---|---|---|
| Tensile strength (MPa) | $17.15 \pm 1.7$ | $21.34 \pm 2.1$ | $24.15 \pm 2.3$ |
| Tensile modulus (MPa) | $10.49 \pm 0.4$ | $18.5 \pm 0.9$ | $28.55 \pm 1.2$ |
| Toughness (MJm$^{-3}$) | $41.8 \pm 5.4$ | $66.4 \pm 6.1$ | $110.8 \pm 5.4$ |
| Elongation at break (%) | $745 \pm 15$ | $936 \pm 35$ | $1090 \pm 50$ |
| Scratch hardness (kg) | $6.1 \pm 0.1$ | $6.5 \pm 0.1$ | $6.8 \pm 0.1$ |
| Impact strength (cm) | >100 | >100 | >100 |

More interestingly, the elongation at the break of the nanocomposites increased with the content of nanohybrid similar to HPU/f-RGO nanocomposites. Such enhancement is due to the alignment of HPU chains in the initial stage of tensile loading, which forces them to orient the nanohybrid along the loading direction as mentioned in HPU/f-RGO nanocomposites (sub-chapter 3C, section 3C.3.4). From **Table 4.1**, a slight deterioration of the mechanical properties of HPU/IO-RGO nanocomposite is observed from the RGO based HPU nanocomposites. This may be due to the presence of a high aspect ratio containing nanomaterial, RGO that provides a mechanically strong nanocomposite.[34] Even though HPU/IO-RGO nanocomposite exhibited better mechanical property than other reported HPU/IO nanocomposites.[35]

### 4.3.6. Thermal properties of HPU/IO-RGO nanocomposite

**Figure 4.10** demonstrates that $T_m$ of the soft segment (PCL moiety) increases upon the incorporation of 2 wt% nanohybrid in HPU matrix. The presence of the nanohybrid may limit the molecular motion of HPU chains in the initial stage.[35] This may be the reason for

the increment of $T_m$. The degree of crystallinity of HPU/IO-RGO nanocomposites increases with the content of the nanohybrid (**Table 4.2**). This clearly suggests that IO-RGO nanohybrid acts as a nucleating agent in the matrix, and thus the presence of the nanohybrid can improve the crystallization process by arranging HPU chains in a particular way.[36]
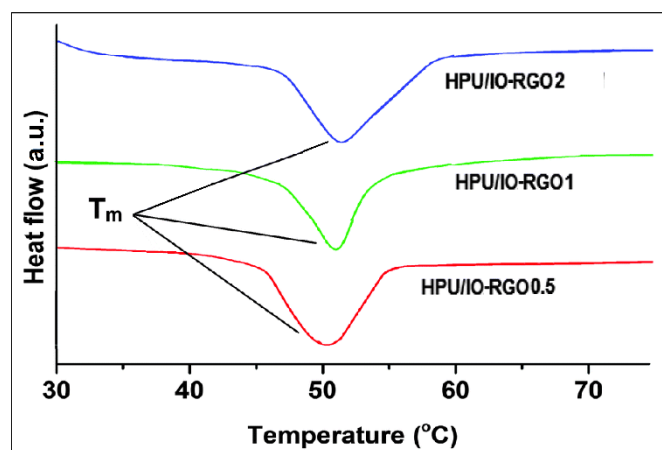


**Figure 4.10** DSC curve showing $T_m$ of the soft segment of HPU/IO-RGO nanocomposite

**Table 4.2** Thermal properties of HPU/IO-RGO nanocomposite

| Property | HPU/IO-RGO0.5 | HPU/IO-RGO1 | HPU/IO-RGO2 |
|----------|---------------|-------------|-------------|
| $T_m$ ($^o$C) | 50.5 | 51.6 | 52.2 |
| Crystallinity (%) | 34.32 | 37.76 | 39.61 |

TGA thermograms of the nanocomposites are shown in **Figure 4.11**. All the thermograms showed two-step degradation patterns similar to HPU (Chapter 2, section 2.3.8). However, the degradation temperatures of the nanocomposites were enhanced compared to HPU. This suggests the good dispersibility of IO-RGO nanohybrid in HPU matrix. The improved thermo-stability of the nanocomposites with the loading of the nanohybrid is due to the limited motion of HPU chains and the presence of different physico-chemical interactions.[37] The produced volatiles during the decomposition were also retained for a longer time in the matrix, due to the better barrier characteristic compared to the pristine HPU.[38]

### 4.3.7. Shape-memory behavior of HPU/IO-RGO nanocomposite

All the nanocomposites exhibited good multi-stimuli responsive shape-memory behavior. Shape-memory behavior of the nanocomposite under MW are shown in **Figure 4.12**. Shape-

memory tests were performed under the exposure of MW and sunlight. The shape-recovery time and ratio under different stimuli are tabulated in **Table 4.3**. In all cases, the shape-recovery time decreased with the increase of nanohybrid content in the nanocomposites. The nanohybrid creates a large amount of stored elastic strain energy, due to the strong interfacial interactions with the compatible HPU matrix.[39] This assists the nanocomposites to achieve a high recovery speed due to the release of this stored elastic strain. Also, the enhancement of the MW and sunlight absorbing capacity with the increase of the nanohybrid content is another important factor for fast recovery. All the nanocomposites demonstrated faster recovery than the corresponding HPU/f-RGO nanocomposite (sub-chapter 3C, Table 3C.3). This is due to presence of IO nanoparticles which possesses excellent MW absorbing capacity and good thermal conductivity.[19]
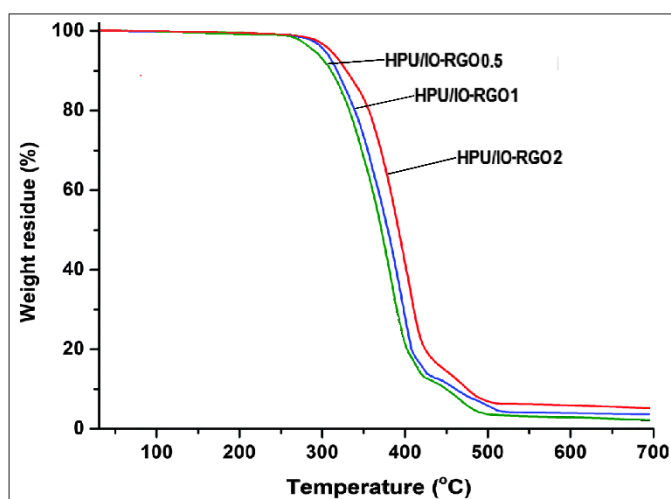


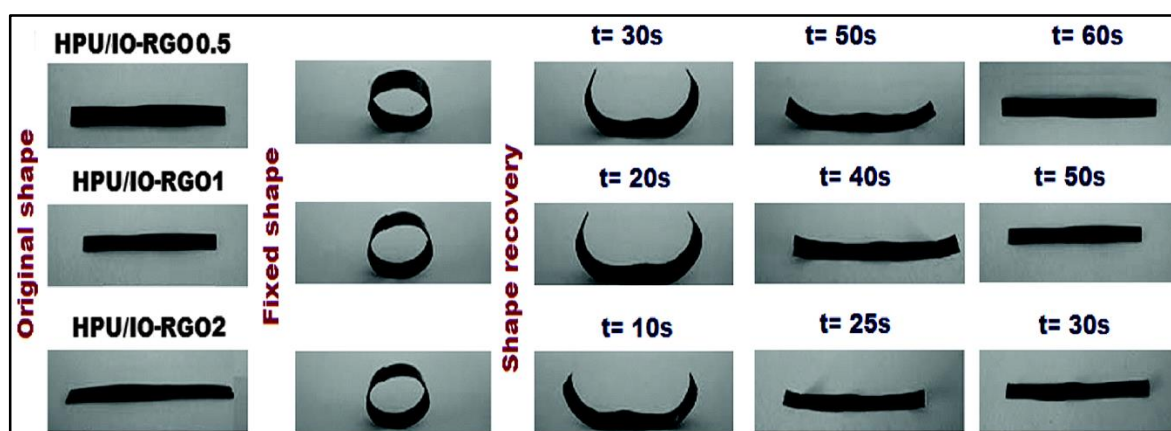**Figure 4.11** TGA thermograms of HPU/IO-RGO nanocomposite



**Figure 4.12** Shape memory behavior of HPU/IO-RGO nanocomposite under MW stimulus

**Table 4.3** Shape memory behavior of HPU/IO-RGO nanocomposite

| Stimulus | Shape memory behavior | HPU/IO-RGO0.5 | HPU/IO-RGO1 | HPU/IO-RGO2 |
|---|---|---|---|---|
| MW | Shape recovery time (min) | $1.03 \pm 0.03$ | $0.88 \pm 0.04$ | $0.51 \pm 0.02$ |
| | Shape recovery ratio (%) | $96.4 \pm 0.2$ | $97.4 \pm 0.2$ | $99.1 \pm 0.1$ |
| Sunlight | Shape recovery time (min) | $2.5 \pm 0.1$ | $2.1 \pm 0.05$ | $1.2 \pm 0.1$ |
| | Shape recovery ratio (%) | $96.1 \pm 0.2$ | $97.2 \pm 0.1$ | $98.5 \pm 0.1$ |

### 4.3.8. Self-healing behavior of HPU/IO-RGO nanocomposite

Optical images were used to examine the healing ability of the nanocomposites. The typical optical images for the flaw film before and after healing are shown in **Figure 4.13**. A comparison of the two optical images before and after the healing clearly demonstrate the completion of the healing process of the nanocomposite film. All the nanocomposites were healed rapidly with excellent healing ability after the incorporation of a small amount (0.5–2 wt%) of IO-RGO nanohybrid.
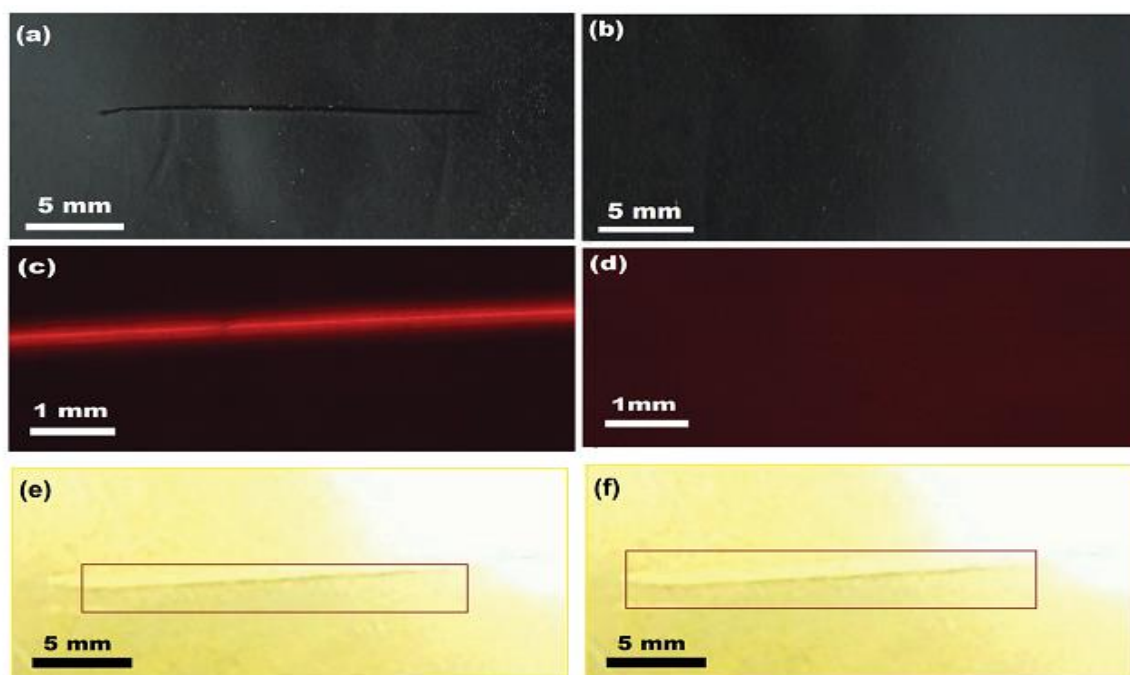


**Figure 4.13** Digital images of (a) cracked nanocomposite film and (b) healed nanocomposite film, and optical microscopic images of (c) cracked nanocomposite film and (d) healed nanocomposite film, and digital images of HPU (e) before and (f) after healing

On the contrary, the pristine HPU film does not heal, or only partially healed, even after long time exposure to any tested stimulus. The incorporation of the nanohybrid remarkably enhanced the healing abilities of HPU, as clearly reflected by this result. The intrinsic properties of IO-RGO nanohybrid, such as excellent MW absorbing capacity and high thermal conductivity, as mentioned earlier, are responsible for this observation.[19]

The healing efficiencies of the nanocomposite films under MW are shown in **Figure 4.14**. This shows that the nanocomposite films were healed with a high healing efficiency of 99% or more. The healing efficiency of the nanocomposite by MW depends on the amount of nanomaterial, MW power input, and the exposure time (**Figure 4.14**a–c). An increased in any of these parameters results in improvements in the healing efficiency. Here, it is pertinent to mention that pristine HPU only slightly healed (10–15%) after 5 min of MW exposure, whereas HPU/RGO nanocomposites were completely healed by MW exposure but required time is quite higher than HPU/IO-RGO nanocomposites.
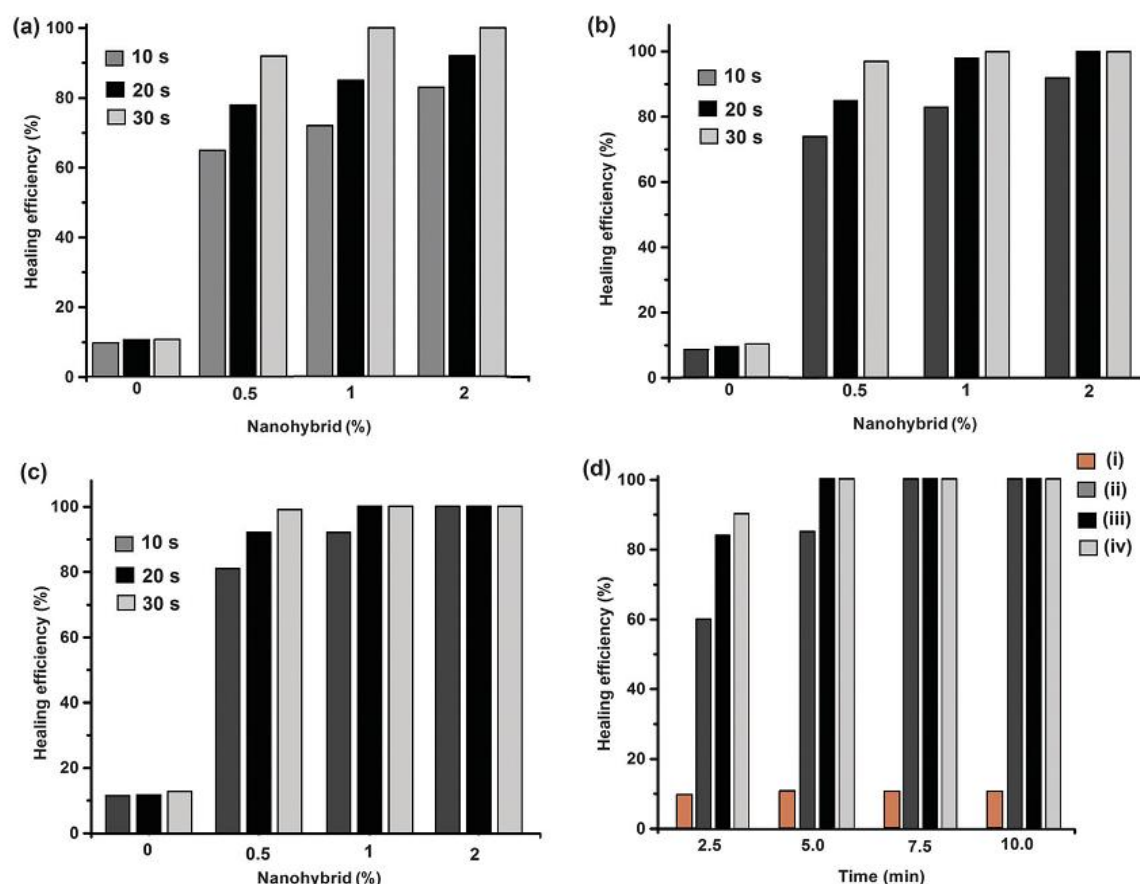


**Figure 4.14** The healing efficiency at MW power of (a) 180 W, (b) 360 W and (c) 540 W, and (d) under direct sunlight for different loadings of nanohybrid (i) 0%, (ii) 0.5%, (iii) 1% and (iv) 2%

The healing of HPU/IO-RGO nanocomposites was faster due to the presence of a high amount of IO in the nanohybrid (an equal amount to RGO), which possesses high MW absorption capacity,[19] and therefore, the nanohybrid absorbs sufficient energy to heal the cracked rapidly. All the nanocomposites were rapidly healed within 20–30 s under low MW power (360 W only). The plausible healing mechanism is shown in **Figure 4.15**. During the healing process, the nanohybrid works as a nanoscale heater, as well as a heat carrier unit. The nanohybrid absorbed MW energy and started to oscillate its dipoles. Heat was generated at the nanohybrid–polymer interface by the friction between the dipoles.[35] The generated heat energy was efficiently transferred to HPU matrix by the nanohybrid, which aided in the rapid Brownian movements of the soft segment of the nanocomposite. Thus, the nanocomposite films were heated uniformly and rapidly upon exposure to a stimulus. This helps to permanently repair the flaw, as diffusion occurs at that flaw site, and also, the process can be repeated multiple times.
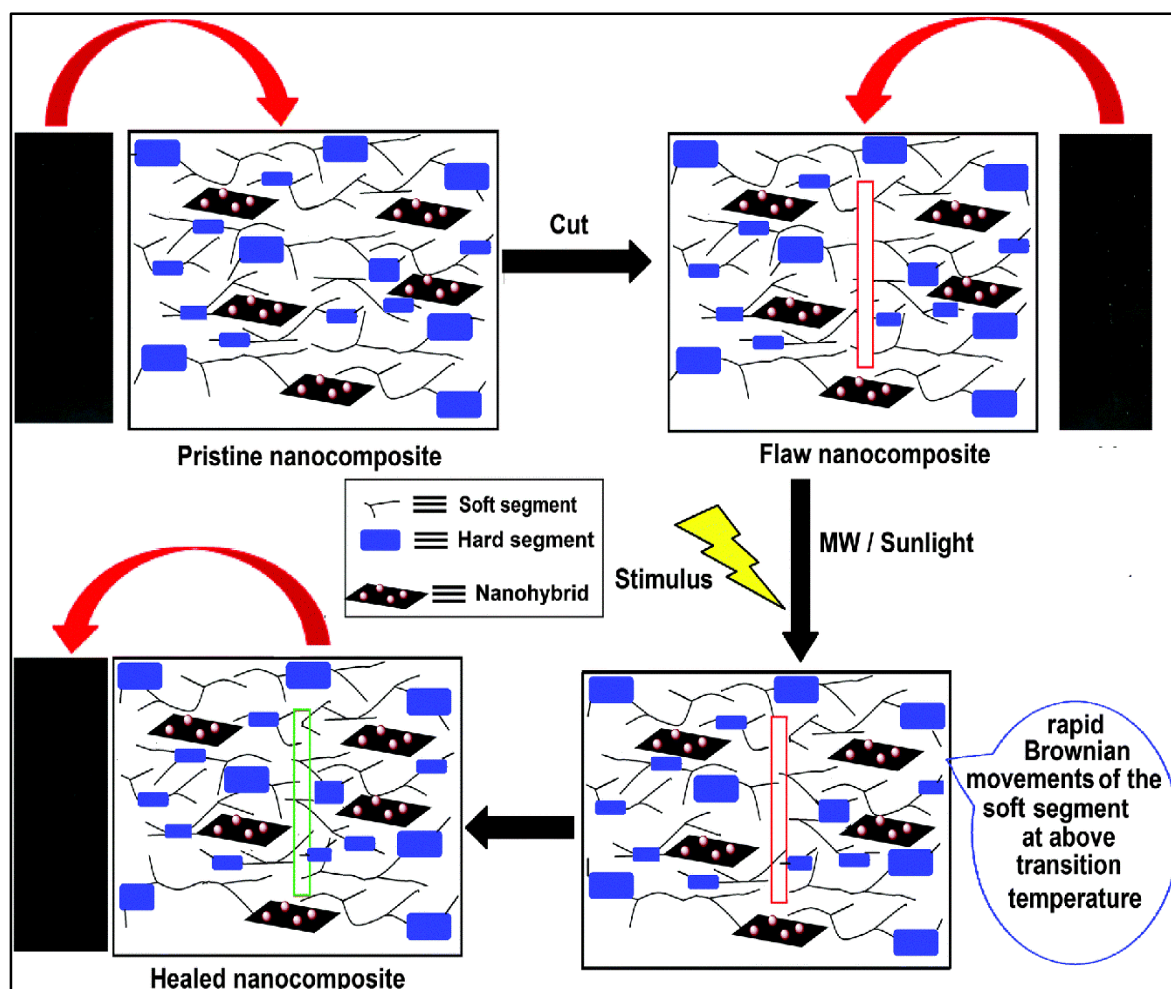


**Figure 4.15** Plausible healing mechanism of HPU/IO-RGO nanocomposite

HPU/IO–RGO2 nanocomposite demonstrated faster healing compared to the other studied HPU/IO-RGO nanocomposites, although it possessed more molecular restriction due to presence of more interactions. This is due to the presence of a higher amount of nanohybrid in it, which helps to absorb more MW energy and helps to transfer this energy to HPU matrix for rapid healing. As self-healing was achieved by the rearrangement and diffusion of the soft segments of HPU, the healing of the prepared nanocomposite could be repeated again and again.[40] As a result, even after the fifth cycle of the experiment, the healing ability of the nanocomposite remains almost the same (**Figure 4.16**).

The nanocomposite with 1% and 2% of nanohybrid demonstrated rapid healing within 5 min, with excellent healing efficiency under direct sunlight exposure (**Figure 4.14**d). But the nanocomposite with 0.5% IO-RGO nanohybrid could only be healed after 7.5 min. These results indicate dose-dependent healing, as well as that this loading of nanohybrid is sufficient for the healing process under sunlight. Similar to MW, the light energy is efficiently transferred throughout the nanocomposite and aids the rapid Brownian movement of the molecular chains of the segment. This causes the rapid healing of the nanocomposite, as diffusion of the chains at the flaw site takes place easily. Here, also the nanocomposite was repeatedly healed by sunlight, and even after the fifth cycle of the experiment, no significant decrease in efficiency was observed (**Figure 4.16**).
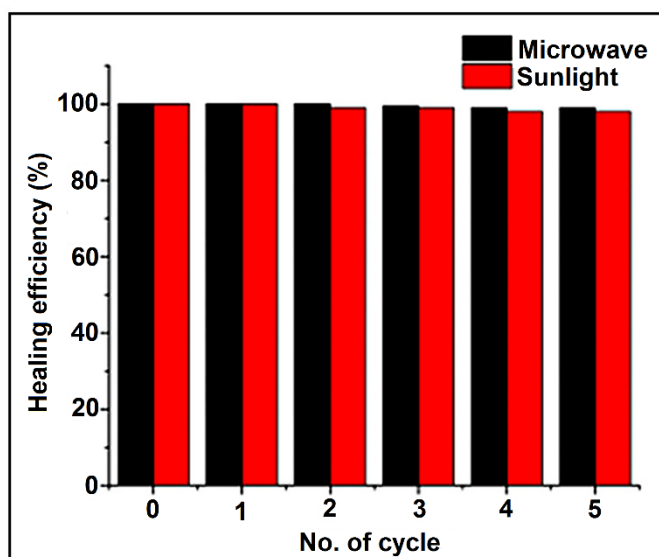


**Figure 4.16** Healing efficiency of HPU/IO–RGO2 for repeated cycles under MW (at 360 W) and sunlight stimuli

Shape memory effect (SME) also helps in the healing process by bringing the polymeric chains in proximity to the crack.[41] Here, it is important to notice that HPU shows a SME but not self-healing ability, although both the processes depend on the rearrangement of the polymeric chains. The energy requirement to activate the polymeric chain for rearranging its orientation and gaining its original shape is less compared with diffusing the polymeric chains in the crack site. A huge amount of energy is needed to soften a particular segment of the polymer and allow subsequent diffusion. Pristine HPU has only one polar group, which is only capable to absorb some energy from the stimulus for rearranging them and return from a deformed state (temporary shape) to their original (permanent) shape. However, this amount of energy may not be sufficient for the polymeric chains diffusion, and as a result pristine HPU only demonstrates SME. In contrast, the IO-RGO nanohybrid possesses good capability to absorb energy from MW and sunlight, and hence nanohybrid absorbs and transfers more amount of the energy to the HPU matrix of the nanocomposite. Therefore, the soft segment of HPU is melted in the nanocomposite and diffuses in the cracked places to heal it.

## 4.4. Conclusion

The study revealed that IO-RGO nanohybrid can be prepared at room temperature by using a greener and one step strategy. The prepared nanohybrid possesses superparamagnetic characteristic with high saturation magnetization value, small coercivity and remanence. Further, the study shown that a self-healable and shape-recoverable HPU nanocomposite with outstanding mechanical properties can be prepared by using IO-RGO nanohybrid as a nanoreinforcing agent. The obtained nanocomposites exhibited a repeatable and rapid healing ability under different stimuli, namely, MW and sunlight, as well as excellent shape-memory behavior under the same stimuli. In contrast to the existing reported self-healing systems, these nanocomposites showed rapid and repeatable healing ability under green stimuli, particularly under sunlight, which is eco-friendly, inexpensive and practically useful. A few more stimuli, such as magnetic, electric and infrared light, may also be used for the same purpose. The nanocomposite shows an enormous potential to be used in various fields such as transport, construction, electronics and so forth.

**References**

1. Varley, R.J., et al. Thermoplastic healing in epoxy networks: Exploring performance and mechanism of alternative healing agents, *Macromol. Mater. Eng.* **298**, 1232--1242, 2013.

2. Wool, R.P. Self-healing materials: a review, *Soft Matter* **4**, 400--418, 2008.

3. Tee, B.C., et al. An electrically and mechanically self-healing composite with pressure- and flexion-sensitive properties for electronic skin applications, *Nat. Nanotechnol.* **7**, 825--832, 2012.

4. Cong, H.P., et al. Stretchable and self-healing graphene oxide–polymer composite hydrogels: a dual-network design, *Chem. Mater.* **25**, 3357--3362, 2013.

5. Jones, A.R., et al. Autonomic healing of carbon fiber/epoxy interfaces, *ACS Appl. Mater. Interfaces* **6** (9), 6033--6039, 2014.

6. Na, X.M., et al. Biodegradable microcapsules prepared by self-healing of porous microspheres, *ACS Macro Lett.* **1**, 697--700, 2012.

7. Lu, Y.X., & Guan, Z. Olefin metathesis for effective polymer healing via dynamic exchange of strong carbon–carbon double bonds, *J. Am. Chem. Soc.* **134**, 14226--14231, 2012.

8. Jin, H., et al. Thermally stable autonomic healing in epoxy using a dual-microcapsule system, *Adv. Mater.* **26**, 282--287, 2014.

9. Koh, E., et al. Microencapsulation of the triazole derivative for self-healing anticorrosion coatings, *New J. Chem.* **38**, 4409--4419, 2014.

10. White, S.R., et al. Autonomic healing of polymer composites, *Nature* **409**, 794--797, 2001.

11. Imbesi, P.M., et al. Model diels–alder studies for the creation of amphiphilic cross-linked networks as healable, antibiofouling coatings, *ACS Macro Lett*. **1**, 473--477, 2012.

12. Trask, R.S., & Bond, I.P. Biomimetic self-healing of advanced composite structures using hollow glass fibres, *Smart Mater. Struct.* **15**, 704--710, 2006.

13. Wu, D.Y., et al. Self-healing polymeric materials: a review of recent developments, *Prog. Polym. Sci.* **33**, 479--522, 2008.

14. Huang, L., et al. Multichannel and repeatable self-healing of mechanical enhanced graphene-thermoplastic polyurethane composites, *Adv. Mater.* **25**, 2224--2228, 2013.

15. Luo, X., & Mather, P.T. Shape memory assisted self-healing coating, *ACS Macro Lett.* **2** (2), 152--156, 2013.

16. Michal, B.T., et al. Inherently photohealable and thermal shape-memory polydisulfide networks, *ACS Macro Lett.* **2**, 694--699, 2013.

17. Wang, X., et al. Improved self-healing of polyethylene/carbon black nanocomposites by their shape memory effect, *J. Phys. Chem. B* **117**, 1467--1474, 2013.

18. Kim, D.K., et al. Energy absorption of superparamagnetic iron oxide nanoparticles by microwave irradiation, *J. Appl. Phys.* **97**, 10J510 (pp 3), 2005.

19. Zhao, X., et al. Excellent microwave absorption property of graphene-coated Fe nanocomposites, *Sci. Rep.* **3**, 3421(pp 5), 2013.

20. Bernardi, M., et al. Extraordinary sunlight absorption and one nanometer thick photovoltaics using two-dimensional monolayer materials, *Nano Lett.* **13** (8), 3664--3670, 2013.

21. Laurent, S., et al. Magnetic iron oxide nanoparticles: Synthesis, stabilization, vectorization, physicochemical characterizations, and biological applications, *Chem. Rev.* **108** (6), 2064--2110, 2008.

22. Qian, W., et al. Surfactant-free hybridization of transition metal oxide nanoparticles with conductive graphene for high-performance supercapacitor, *Green Chem.* **14**, 371--377, 2012.

23. Wu, H., et al. Control on the formation of $Fe_3O_4$ nanoparticles on chemically reduced graphene oxide surfaces, *Cryst. Eng. Comm.* **14**, 499--504, 2012.

24. Yang, X., et al. Superparamagnetic graphene oxide–$Fe_3O_4$ nanoparticles hybrid for controlled targeted drug carriers, *J. Mater. Chem.* **19**, 2710--2714, 2009.

25. Ji, L., et al. Facile synthesis of multiwall carbon nanotubes/iron oxides for removal of tetrabromobisphenol A and Pb(II), *J. Mater. Chem.* **22**, 15853--15862, 2012.

26. Akhavan, O., et al. Increasing the antioxidant activity of green tea polyphenols in the presence of iron for the reduction of graphene oxide, *Carbon* **50**, 3015--3025, 2012.

27. Xie, G., et al. A facile chemical method to produce superparamagnetic graphene oxide–$Fe_3O_4$ hybrid composite and its application in the removal of dyes from aqueous solution, *J. Mater. Chem.* **22**, 1033--1039, 2012.

28. Das, B., et al. Nanocomposites of bio-based hyperbranched polyurethane/funtionalized MWCNT as non-immunogenic, osteoconductive, biodegradable and biocompatible scaffolds in bone tissue engineering, *J. Mater. Chem. B* **1**, 4115--4126, 2013.

29. Das, B., et al. Bio-based hyperbranched polyurethane/$Fe_3O_4$ nanocomposites: Smart antibacterial biomaterials for biomedical devices and implants, *Biomed. Mater.* **8**, 035003 (pp 12), 2013.

30. Chen, T., et al. Achieving high performance electric field induced strain: a rational design of hyperbranched aromatic polyamide functionalized graphene–polyurethane dielectric elastomer composites, *J. Phys. Chem. B* **119** (12), 4521--4530, 2015.

31. Chen, Z., & Lu, H. Constructing sacrificial bonds and hidden lengths for ductile graphene/polyurethane elastomers with improved strength and toughness, *J. Mater. Chem.* **22**, 12479--12490, 2012.

32. Cai, D., et al. High performance polyurethane/functionalized graphene nanocomposites with improved mechanical and thermal properties, *Compos. Sci. Technol.* **6**, 702--707, 2012.

33. Pei, A., et al. Strong nanocomposite reinforcement effects in polyurethane elastomer with low volume fraction of cellulose nanocrystals, *Macromolecules* **44** (11), 4422--4427, 2011.

34. Yoo, H.J., et al. High-speed actuation and mechanical properties of graphene-incorporated shape memory polyurethane nanofibers, *J. Phys. Chem. C* **118** (19), 10408--10415, 2014.

35. Kalita, H., & Karak, N. Bio-based hyperbranched polyurethane/$Fe_3O_4$ nanocomposites as shape memory materials, *Polym. Adv. Technol.* **24**, 819--823, 2013.

36. Hodlur R.M., & Rabinal, M.K. Self assembled graphene layers on polyurethane foam as a highly pressure sensitive conducting composite, *Compos. Sci. Technol.* **90**, 160--165, 2014.

37. Layek, R.K., et al. High-performance nanocomposites of sodium carboxy-methylcellulose and graphene oxide, *Macromol. Mater. Eng.* **298**, 1166--1175, 2013.

38. Jeong, E.H., et al. Effective preparation and characterization of montmorillonite/poly(ε-caprolactone)-based polyurethane nanocomposites, *J. Appl. Polym. Sci.* **107**, 803--809, 2008.

39. Deka, H., et al. Biocompatible hyperbranched polyurethane/multi-walled carbon nanotube composites as shape memory materials, *Carbon* **48**, 2013--2022, 2010.

40. Bai, Y., et al. Poly(vinyl butyral) based polymer networks with dual-responsive shape memory and self-healing properties, *J. Mater. Chem. A* **2**, 9169--9177, 2014.

41. Luo, X., & Mather, P.T. Shape memory assisted self-healing coating, *ACS Macro Lett.* **2** (2), 152--156, 2013.